Imaging Magnetization Structure and Dynamics in Ultrathin Y_{3}Fe_{5}O_{12}/Pt Bilayers with High Sensitivity Using the Time-Resolved Longitudinal Spin Seebeck Effect

Jason M. Bartell, Colin L. Jermain, Sriharsha V. Aradhya, Jack T. Brangham, Fengyuan Yang, Daniel C. Ralph, and Gregory D. Fuchs

Phys. Rev. Applied **7**, 044004 — Published 6 April 2017

DOI: 10.1103/PhysRevApplied.7.044004

Imaging Magnetization Structure and Dynamics in Ultrathin YIG/Pt Bilayers with High Sensitivity Using the Time-Resolved Longitudinal Spin Seebeck Effect

Jason M. Bartell[1], Colin L. Jermain[1], Sriharsha V. Aradhya[1], Jack T. Brangham[2], Fengyuan Yang[2], Daniel C. Ralph[1,3], Gregory D. Fuchs[1]

[1]Cornell University, Ithaca, NY 14853, USA

[2]Department of Physics, The Ohio State University, Columbus, OH 43016, USA

[3]Kavli Institute at Cornell for Nanoscale Science, Ithaca, NY 14853, USA

ABSTRACT

We demonstrate an instrument for time-resolved magnetic imaging that is highly sensitive to the in-plane magnetization state and dynamics of thin-film bilayers of yttrium iron garnet ($Y_3Fe_5O_{12}$, YIG)/Pt: the time-resolved longitudinal spin Seebeck (TRLSSE) effect microscope. We detect the local, in-plane magnetic orientation within the YIG by focusing a picosecond laser to generate thermally-driven spin current from the YIG into the Pt by the spin Seebeck effect, and then use the inverse spin Hall effect in the Pt to transduce this spin current to an output voltage. To establish the time resolution of TRLSSE, we show that pulsed optical heating of patterned YIG (20 nm)/Pt(6 nm)/Ru (2 nm) wires generates a magnetization-dependent voltage pulse of less than 100 ps. We demonstrate TRLSSE microscopy to image both static magnetic structure and gigahertz-frequency magnetic resonance dynamics with sub-micron spatial resolution and a sensitivity to magnetic orientation below 0.3 deg/$\sqrt{Hz}$ in ultrathin YIG.

I. INTRODUCTION

Ultrathin bilayers of the magnetic insulator YIG interfaced with a heavy, non-magnetic metal (NM) such at Pt are being intensely studied for the development of high-efficiency magnetic memory and logic devices operated by spin-orbit torque [1,2], for magnon generation and propagation [3–5], and as a model system for understanding spin-current generation by the longitudinal spin Seebeck effect (LSSE) and spin pumping [6–9]. For all of these research areas, it would be useful to have a high-sensitivity and local probe of magnetization dynamics in the YIG layer, especially for the ultrathin films required in many devices. This has proven challenging, and although magneto-optical techniques such as Brillouin light scattering and the magneto-optical Kerr effect (MOKE) have proven valuable [3,10–14], they have not enabled direct time-resolved imaging of magnetic precession or direct imaging of in-plane magnetization of ultra-thin YIG films (20 nm and below). An alternative approach that enables in-plane imaging of YIG/Pt bilayer devices was demonstrated by Weiler *et al*. [15]. In that work, the authors use laser heating to image the in-plane magnetic structure of YIG, but not its dynamics. Here we extend the approach into the time domain to perform high sensitivity imaging of the in-plane magnetic orientation ($< 0.3°/\sqrt{Hz}$) with sub-micron spatial resolution and sub-100 ps temporal resolution. Using TRLSSE microscopy we can observe, for example, that the resonance field in ultra-thin YIG films can vary by up to 30 Oe within micron-scale regions of a YIG/Pt device. Our results demonstrate that TRLSSE microscopy is a powerful tool to characterize static and dynamic magnetic properties in ultrathin YIG.

The principle behind the TRLSSE microscope, shown schematically in Fig. 1, is the generation and detection of a thermally generated local spin current [16]. For the case of YIG/Pt, a local thermal gradient perpendicular to the film plane is generated by laser heating of Pt. The

gradient creates a thermally-induced spin current that is proportional to the local magnetization [17–19]. The spin current that flows into the Pt is detected with the ISHE [20,21] in which spin-orbit coupling leads to a spin-dependent transverse electric field. For this work, the resulting voltage can be described as [17,19] $V_{LSSE} \propto -\xi_{SH} S \frac{\mathbf{M}(\boldsymbol{x},t)}{M_s} \times \boldsymbol{\nabla}\mathbf{T}(\boldsymbol{x},t)$, where, ξ_{SH} is the spin Hall efficiency, S is the spin-Seebeck coefficient, $\mathbf{M}$ is the local magnetization, M_s is the saturation magnetization and $\boldsymbol{\nabla}\mathbf{T}$ is the thermal gradient. The LSSE has been attributed to both thermal gradients across the thickness of YIG and to interfacial temperature differences between YIG and Pt [17–19,22,23]. Our experiment cannot definitively distinguish between these two mechanisms. Thus, here we discuss only $\boldsymbol{\nabla}\mathbf{T}$ as single quantity for simplicity and for consistency with our prior work using the anomalous Nernst effect, however, this question requires further study. V_{LSSE} is a read-out of the local magnetization m_y because the electric field is generated in response to the spatially local z-component of the thermal gradient, ∇T_z (coordinates as defined in Fig. 1) [15,24].

To extend LSSE imaging into the time-domain, we use picosecond laser heating to stroboscopically sample magnetization. We have previously shown [25], in metallic ferromagnets, that picosecond heating can be used for stroboscopic magnetic microscopy using the time-resolved anomalous Nernst effect (TRANE). In TRANE microscopy, the temporal resolution is set by the excitation and decay of a thermal gradient within a single material that both absorbs the heat from the laser pulse and produces a TRANE voltage from internal spin-orbit interactions [26,27]. In the LSSE however, the timescale of spin current generation can depend on both the timescale of the thermal gradient and the timescale of energy transfer between the phonons and magnons. Recent experiments indicate that in the qausi-static regime the magnon-phonon relaxation rate may play a dominant role [28–31]. Using picosecond heating

and time-resolved electrical detection to move beyond the quasi-static regime, we show a TRLSSE in agreement with a recent all-optical experiment [22].

II. DESCRIPTION OF EXPERIMENT

We grew our samples using off-axis sputtering onto (110)-oriented gadollinum gallium garnet ($Gd_3Ga_5O_{12}$, GGG), [32–34] followed by *ex situ.* deposition of 6 nm of Pt with a 2 nm Ru capping layer. Photolithography and ion milling were used to pattern wires and contacts for wirebonding. We present measurements of a 2 μm × 10 μm wire and a 4 μm × 10 μm wire with DC resistances of 296 Ω and 111 Ω respectively. In this room temperature study, we neglect the potential anomalous Nernst effect of interfacial Pt with induced magnetization [35,36], and we neglect a possible photo-spin voltaic effect [37], neither of which can be distinguished from TRLSSE in presented measurements.

Our TRLSSE measurement consists of pulsed laser heating and homodyne electrical detection as shown in Fig. 2a. We use a Ti:Sapphire laser pulse to locally heat the sample with 3 ps pulses of 780 nm light at a repetition rate of 25.5 MHz. The electrical signal produced at the sample is the sum of the LSSE dependent voltage, $V_{LSSE}(\nabla T_z, \mathbf{M})$, and a voltage, $V_J(\Delta T, J)$, which is generated when a current density J is passing through the local region of Pt with increased resistance due to laser heating [38]. To reject noise and recover the signal of the resulting electrical pulses, we use a time-domain homodyne technique in which we mix the $V_{LSSE} + V_J$ pulse train with a synchronized reference pulse train, V_{mix}, in a broadband (0.1-12 GHz) electrical mixer. The mixer output is the convolution of the two pulse trains given by [38]

$$V_{sig}(\boldsymbol{x}, \tau) = K \int_0^{\Gamma} (V_{LSSE}(\nabla T_z(\boldsymbol{x}, t), \mathbf{M}(\boldsymbol{x}, t)) + V_J(\Delta T(\boldsymbol{x}, t), J(\boldsymbol{x}, t))\, V_{mix}(\tau - t) dt, \qquad (1)$$

where $\boldsymbol{x}(x,y)$ is the laser spot position in the sample plane, Γ is the period of the laser pulses, K is the transfer coefficient, and τ is the relative delay. A relative delay of zero corresponds to the maximum of both pulse trains arriving at the mixer simultaneously.

We study the timescale of the LSSE signal generated by a picosecond pulse by measuring V_{sig} as a function of mixer delay τ. Fig. 2b shows the result of this measurement using a 100 ps mixing pulse reference, V_{mix}, at a saturating magnetic field, H, perpendicular to the wire at H = +414 Oe and – 414 Oe, respectively. In Figure 2c we plot the difference between these two voltage traces to reject non-magnetic contributions. We find that the full-width at half-maximum (FWHM) is 100±10 ps, which is followed by electrical oscillations that we attribute to non-idealities in the detection circuit (see the SI for further discussion [39].) Because the duration of the magnetic component of V_{sig} is experimentally indistinguishable from the FWHM of V_{mix}, we conclude that 100 ps is an experimental upper bound for the TRLSSE signal duration.

To calibrate the local change in the Pt temperature, ΔT_{Pt}, due to picosecond heating and to quantify the rate of thermal relaxation, we measure V_J in the presence of a DC current, which uses the local Pt resistivity as an ultra-fast thermometer. Figure 2d shows V_J as a function of mixer delay, $V_J(\tau) = V_{sig}(\tau, J = 4.2\ \mathrm{MA/cm^2}) - V_{sig}(\tau, J = -4.2\ \mathrm{MA/cm^2})$, for applied currents of ±0.5 mA. $V_J(\tau)$ is proportional to ΔT_{pt} through V_J, but it is not proportional to either the magnetic state of the sample or ∇T_z. We observe that V_J relaxes to zero faster than the laser repetition period, indicating that the sample thermally recovers between pulses. To quantitatively consider the spatiotemporal thermal evolution, we performed a time-domain finite element (TDFE) calculation of focused laser heating in the wire. Additional details are available in the SI [39], and see Ref. [25] for a lengthier discussion of the procedure. The comparison of the spatiotemporal profile of the calculation and the known temperature dependence of resistivity

enable us to calibrate the spatiotemporal temperature rise due to laser heating. We find that the peak film temperature changes by ~50 K in the platinum and ~ 10 K in the YIG for a laser fluence of 5.8 mJ/cm^2, which is the maximum for the presented measurements [40–44]. Note that we assume all laser heating is mediated by optical absorption in Pt because YIG and GGG are transparent at 780 nm [45,46]. The TDFE calculation reveals that, in agreement with experiment, ∇T_z across the YIG thickness decays more quickly than the full thermal relaxation of the Pt back to the ambient temperature (e.g. $\Delta T_{pt} = 0$). This difference in timescales between ∇T_z and ΔT_{pt} is important because the magnetic signal in our experiment is sensitive to only $\nabla T_z(t)$, not $\Delta T_{pt}(t)$ of the Pt.

III. STROBOSCOPIC MEASUREMENT OF FERROMAGNETIC RESONANCE

The sub-100 ps spin current lifetime in our experiment is short enough that the TRLSSE is useful for stroboscopic measurements of resonant YIG magnetization dynamics. To confirm this idea, we use TRLSSE microscopy to measure ferromagnetic resonance (FMR) by driving a gigahertz-frequency a.c. current into the Pt, which generates magnetic torques on YIG from both the Oersted magnetic field and from spin currents generated by the spin Hall effect [47–49]. The current is generated with an arbitrary waveform generator (AWG) that is phase-locked to the laser repetition rate and coupled to the YIG/Pt device through a circulator (see schematic in Fig. 3a). Synchronizing the a.c. current and the laser repetition rate ensures a constant but controllable phase between the precessing magnetization and the sensing heat pulse for a given driving frequency and magnetic field. In our FMR measurements, we fix $\tau = 0$ and align the wire axis parallel to the external magnetic field. In this configuration, the TRLSSE signal is stroboscopically sensitive to the magnetic projection m_y at a particular phase of the magnetic precession about the x-axis. In addition to V_{LSSE}, V_{sig} contains a contribution from V_J that is

proportional to the local a.c. current amplitude and phase [38]. We separate the magnetic V_{LSSE} from the non-magnetic V_J by measuring V_{sig} with a lock-in amplifier referenced to a 383 Hz, 7.6 Oe RMS modulation of the external magnetic field. Fig. 3b shows LSSE FMR spectra as a function of field excited using a 1.2 ± 0.3 mA and 1.4 ± 0.4 mA a.c. current at 4.1 GHz and 4.9 GHz respectively. In the limit that the modulation magnetic field is small compared to the FMR linewidth, we can interpret the resulting signal V_{mod} as a derivative signal that contains a linear combination of the real and imaginary parts of the dynamic susceptibility, χ, $V_{mod}(H) \propto \frac{d\chi'}{dH}Sin(\theta) + \frac{d\chi''}{dH}Cos(\theta)$. This relation is used to fit the FMR spectra to extract the amplitude, phase, linewidth, and resonant field. For more details on fitting see refs [25,38]. To demonstrate that the TRLSSE microscope is a phase-sensitive stroboscope, we rotated the phase of the microwave current by 180° and re-measure FMR. As expected, inverting the phase of the drive inverts the phase of the FMR lineshape (Fig. 3c).

IV. CHARACTERIZATION OF SENSITIVITY

Next, we quantify the sensitivity of TRLSSE microscopy for our ultra-thin YIG/Pt samples. Figure 4 shows representative LSSE measurements of the YIG magnetization versus magnetic field perpendicular to the wire at several optical powers. In this geometry, the positive and negative saturation values of V_{LSSE} quantify the full range of magnetization, $+M$ to $-M$. Then, using the standard deviation of the noise in the LSSE voltage, σ_{LSSE}, we can quantify the angular sensitivity noise floor assuming small angle magnetic deviations from the wire axis, such as for stroboscopic FMR measurements. The sensitivity is calculated using [25] $\theta_{\min} = \frac{\sigma_{\mathrm{LSSE}}}{\sin(\theta_{\mathrm{o}})(V_{\mathrm{LSSE}}^{\max} - V_{\mathrm{LSSE}}^{\min})/2}\sqrt{TC}$ where TC is the lock-in time constant. We find a sensitivity of 0.3 deg/√Hz for an optical power of 0.6 mW, corresponding to a laser fluence of 5.8 mJ/cm^2. It is

155 important to note that the sensitivity is sample dependent through both sample geometry and the
156 impedance match with the detection circuit [25].

157 The interface quality of the sample plays a key role in determining the sensitivity. As spin
158 current diffuses into the platinum, it is subject to loss at the interface. A good indication of
159 interfacial spin transparency is the spin Hall magnetoresistance (SMR) [50,51], which is
160 sensitive to the spin mixing conductance at the interface. For the data presented here, the devices
161 show a SMR of 0.063%, which is the largest value by a factor of 2 from the other devices we
162 patterned. This is consistent with a number of recent SMR reports [50–54], and we expect the
163 high SMR value indicates strong spin transparency at the YIG/Pt interface. We also studied
164 YIG/Pt samples with no measureable SMR which we expect to have a significantly reduced
165 LSSE induced ISHE voltage. We found that the LSSE signal in these devices is approximately
166 an order of magnitude lower for the same laser fluence. Additional details are in the SI [39].

167 V. IMAGING STATIC AND DYNAMIC MAGNETIZATION

168 Having placed upper bounds on the time resolution and quantified the sensitivity, next we
169 demonstrate the application of TRLSSE microscopy for imaging of static magnetization. We
170 acquire images by scanning the laser focus and making a point-by-point measurement of the
171 TRLSSE voltage and reflected light. Figures 5a and 5b show a reflected light image and
172 saturated LSSE image, respectively, for a 4 μm wide YIG/Pt device. In the reflection image, we
173 see the structure of the wire and the contact pads at both ends. We acquired the TRLSSE image
174 at H =–405 Oe and shifted the background level for clarity of the color scale. No other image
175 processing was performed. We observe a uniform magnetization state of the YIG/Pt device, as
176 expected from the previously presented magnetic hysteresis measurements (Fig. 4). When we
177 reduce the field to near zero (H = 4 Oe) and re-image the wire (Fig. 5c), magnetic texture is

178 revealed that indicates non-uniform canting of the device magnetization. To more clearly show
179 the variation in contrast between images, we plot line cuts of Figs. 5a-c in Fig. 5d. Despite the
180 inhomogeneous remanence that is evident in Fig. 5c, we were not able to observe domains with
181 oppositely aligned magnetization; possibly because once a reversal domain is nucleated, the
182 domain wall propagates without strong pinning.

183 Without a 180^{o} domain wall the spatial resolution of TRLSSE cannot be directly evaluated.
184 Nevertheless, we use the reflected light image and TDFE simulations to study the possibility that
185 lateral thermal spreading degrades the resolution. To approximate the lateral point spread
186 function of the laser, we fit a scan of the wire step edge to a Gaussian point spread function. This
187 yields a spot FWHM of 0.606 μm. Calculations of the heating indicate that the thermal gradient
188 does not spread laterally in the Pt, thus we expect that the resolution of the TRLSSE is the same
189 as the diffraction-limited optical resolution in this experiment.

190 We now demonstrate that TRLSSE microscopy has the sensitivity to image dynamic
191 magnetization in the 4 μm YIG/Pt device, which provides quantitative and spatially localized
192 information about dynamical properties of ultrathin YIG materials. As described above, for
193 FMR characterization we orient the external magnetic field parallel to the wire axis and drive a
194 1.2 ± 0.1 mA, 4.9 GHz current into the wire. We image dynamical magnetization at a series of
195 magnetic fields near the resonance field, from H = 896 Oe to 1105 Oe, and plot a selection of the
196 unprocessed images in Figs. 5e-g. The data show that at H far from resonance (Fig. 5e) where
197 precession amplitudes are tiny, the TRLSSE signal at the center of the wire is well below the
198 detection noise floor. There is a small, current-induced, non-magnetic signal artifact at the edges
199 of the wire which we discuss further in the supplemental information [39]. For H near the
200 resonant field, H_{res}, the device has a strong, position-dependent TRLSSE response. To

quantitatively analyze the data, images are corrected for background offset and sample drift before fitting a resonance field curve for each pixel. We plot a selection of curves from individual pixels in Fig. 6a. We then construct a spatial map of each fitting parameter: H_{res}, relative phase, ϕ, amplitude, A, and linewidth, ΔH, and offset, all of which are shown in Fig. 6b-f. We immediately notice spatial variation in these images that is qualitatively similar to the non-uniform magnetic remanence texture shown in Fig. 5c. Together, these measurements confirm the presence of varying local magnetic anisotropy and quantify both static and dynamic magnetic properties in each region. The ability to quantitatively relate the spatial variation of static and dynamic properties in ultrathin YIG/Pt devices is a unique capability of our microscope.

VI. CONCLUSION

In conclusion, we have demonstrated sensitive and high-resolution TRLSSE microscopy of ultrathin YIG/Pt devices that we expect will prove useful for developing spintronic applications. Using picosecond heating, we demonstrate that TRLSSE microscopy is a sub-100 picosecond probe of ultra-thin YIG/Pt device magnetization, both for static magnetic configurations and for dynamical measurements at gigahertz frequencies. We have demonstrated an angular sensitivity of $0.3°/\sqrt{Hz}$, making it one of the most sensitive experimental probes of ultra-thin YIG magnetic orientation.

ACKNOWLEDGMENTS

We thank J. Kimling and D. G. Cahill for helpful comments on an early version of the manuscript, and for providing the interface thermal resistance of YIG/Pt. This research was supported by the U.S. Air Force Office of Scientific Research, under Contract No. FA9550-14-1-0243, and by U.S. National Science Foundation under Grants No. DMR-1406333 and DMR-1507274 and through the Cornell Center for Materials Research (CCMR) (DMR-1120296). This

work made use of the CCMR Shared Facilities and the Cornell NanoScale Facility, a member of the National Nanotechnology Coordinated Infrastructure, which is supported by the NSF (Grant No. ECCS-1542081).

REFERENCES

[1] B. Behin-Aein, D. Datta, S. Salahuddin, and S. Datta, Proposal for an all-spin logic device with built-in memory, Nat. Nanotechnol. **5**, 266 (2010).

[2] K. Ganzhorn, S. Klingler, T. Wimmer, S. Geprägs, R. Gross, H. Huebl, and S. T. B. Goennenwein, Magnon-based logic in a multi-terminal YIG/Pt nanostructure, Appl. Phys. Lett. **109**, 022405 (2016).

[3] C. W. Sandweg, Y. Kajiwara, A. V. Chumak, a. a. Serga, V. I. Vasyuchka, M. B. Jungfleisch, E. Saitoh, and B. Hillebrands, Spin Pumping by Parametrically Excited Exchange Magnons, Phys. Rev. Lett. **106**, 216601 (2011).

[4] H. Kurebayashi, O. Dzyapko, V. E. Demidov, D. Fang, A. J. Ferguson, and S. O. Demokritov, Controlled enhancement of spin-current emission by three-magnon splitting., Nat. Mater. **10**, 660 (2011).

[5] P. Pirro, T. Brächer, A. V. Chumak, B. Lägel, C. Dubs, O. Surzhenko, P. Görnert, B. Leven, and B. Hillebrands, Spin-wave excitation and propagation in microstructured waveguides of yttrium iron garnet/Pt bilayers, Appl. Phys. Lett. **104**, 012402 (2014).

[6] K. Uchida, J. Xiao, H. Adachi, J. Ohe, S. Takahashi, J. Ieda, T. Ota, Y. Kajiwara, H. Umezawa, H. Kawai, G. E. W. Bauer, S. Maekawa, and E. Saitoh, Spin Seebeck insulator, Nat. Mater. **9**, 894 (2010).

[7] K. Uchida, H. Adachi, T. An, T. Ota, M. Toda, B. Hillebrands, S. Maekawa, and E. Saitoh, Long-range spin Seebeck effect and acoustic spin pumping., Nat. Mater. **10**, 737 (2011).

[8] G. E. W. Bauer, E. Saitoh, and B. J. van Wees, Spin caloritronics., Nat. Mater. **11**, 391 (2012).

[9] S. R. Boona, R. C. Myers, and J. P. Heremans, Spin caloritronics, Energy Environ. Sci. **7**, 885 (2014).

[10] V. E. Demidov, M. Evelt, V. Bessonov, S. O. Demokritov, J. L. Prieto, M. Muñoz, J. Ben Youssef, V. V. Naletov, G. de Loubens, O. Klein, M. Collet, P. Bortolotti, V. Cros, and A. Anane, Direct observation of dynamic modes excited in a magnetic insulator by pure spin current, Sci. Rep. **6**, 32781 (2016).

[11] D. A. Bozhko, A. A. Serga, P. Clausen, V. I. Vasyuchka, F. Heussner, G. A. Melkov, A. Pomyalov, V. S. L'vov, and B. Hillebrands, Supercurrent in a room-temperature Bose–Einstein magnon condensate, Nat. Phys. **12**, 1057 (2016).

[12] M. B. Jungfleisch, W. Zhang, J. Sklenar, J. Ding, W. Jiang, H. Chang, F. Y. Fradin, J. E. Pearson, J. B. Ketterson, V. Novosad, M. Wu, and A. Hoffmann, Large Spin-Wave Bullet in a Ferrimagnetic Insulator Driven by the Spin Hall Effect, Phys. Rev. Lett. **116**, 057601 (2016).

[13] K. An, K. S. Olsson, A. Weathers, S. Sullivan, X. Chen, X. X. Li, L. G. Marshall, X. Ma,

N. Klimovich, J. Zhou, L. Shi, and X. X. Li, Magnons and Phonons Optically Driven out of Local Equilibrium in a Magnetic Insulator, Phys. Rev. Lett. **117**, 107202 (2016).

[14] M. Montazeri, P. Upadhyaya, M. C. Onbasli, G. Yu, K. L. Wong, M. Lang, Y. Fan, X. Li, P. Khalili Amiri, R. N. Schwartz, C. A. Ross, and K. L. Wang, Magneto-optical investigation of spin–orbit torques in metallic and insulating magnetic heterostructures, Nat. Commun. **6**, 8958 (2015).

[15] M. Weiler, M. Althammer, F. D. Czeschka, H. Huebl, M. S. Wagner, M. Opel, I.-M. Imort, G. Reiss, A. Thomas, R. Gross, and S. T. B. Goennenwein, Local Charge and Spin Currents in Magnetothermal Landscapes, Phys. Rev. Lett. **108**, 106602 (2012).

[16] Y. Kajiwara, K. Harii, S. Takahashi, J. Ohe, K. Uchida, M. Mizuguchi, H. Umezawa, H. Kawai, K. Ando, K. Takanashi, S. Maekawa, and E. Saitoh, Transmission of electrical signals by spin-wave interconversion in a magnetic insulator, Nature **464**, 262 (2010).

[17] J. Xiao, G. E. W. Bauer, K. Uchida, E. Saitoh, and S. Maekawa, Theory of magnon-driven spin Seebeck effect, Phys. Rev. B **81**, 214418 (2010).

[18] S. M. Rezende, R. L. Rodríguez-Suárez, R. O. Cunha, a. R. Rodrigues, F. L. A. Machado, G. a. Fonseca Guerra, J. C. Lopez Ortiz, and A. Azevedo, Magnon spin-current theory for the longitudinal spin-Seebeck effect, Phys. Rev. B **89**, 014416 (2014).

[19] M. Schreier, A. Kamra, M. Weiler, J. Xiao, G. E. W. Bauer, R. Gross, and S. T. B. Goennenwein, Magnon, phonon, and electron temperature profiles and the spin Seebeck effect in magnetic insulator/normal metal hybrid structures, Phys. Rev. B **88**, 094410 (2013).

[20] K. Uchida, H. Adachi, T. Ota, H. Nakayama, S. Maekawa, and E. Saitoh, Observation of longitudinal spin-Seebeck effect in magnetic insulators, Appl. Phys. Lett. **97**, 172505 (2010).

[21] C. M. Jaworski, J. Yang, S. Mack, D. D. Awschalom, J. P. Heremans, and R. C. Myers, Observation of the spin-Seebeck effect in a ferromagnetic semiconductor, Nat. Mater. **9**, 898 (2010).

[22] J. Kimling, G.-M. Choi, J. T. Brangham, T. Matalla-Wagner, T. Huebner, T. Kuschel, F. Yang, and D. G. Cahill, Picosecond Spin Seebeck Effect, Phys. Rev. Lett. **118**, 057201 (2017).

[23] S. Hoffman, K. Sato, and Y. Tserkovnyak, Landau-Lifshitz theory of the longitudinal spin Seebeck effect, Phys. Rev. B **88**, 064408 (2013).

[24] A. von Bieren, F. Brandl, D. Grundler, and J.-P. Ansermet, Space- and time-resolved Seebeck and Nernst voltages in laser-heated permalloy/gold microstructures, Appl. Phys. Lett. **102**, 052408 (2013).

[25] J. M. Bartell, D. H. Ngai, Z. Leng, and G. D. Fuchs, Towards a table-top microscope for nanoscale magnetic imaging using picosecond thermal gradients, Nat. Commun. **6**, 8460 (2015).

[26] T. Miyasato, N. Abe, T. Fujii, a. Asamitsu, S. Onoda, Y. Onose, N. Nagaosa, and Y. Tokura, Crossover Behavior of the Anomalous Hall Effect and Anomalous Nernst Effect in Itinerant Ferromagnets, Phys. Rev. Lett. **99**, 086602 (2007).

[27] N. Nagaosa, J. Sinova, S. Onoda, A. H. MacDonald, and N. P. Ong, Anomalous Hall effect, Rev. Mod. Phys. **82**, 1539 (2010).

[28] M. Schreier, F. Kramer, H. Huebl, S. Geprägs, R. Gross, S. T. B. Goennenwein, T. Noack, T. Langner, A. A. Serga, B. Hillebrands, and V. I. Vasyuchka, Spin Seebeck effect at microwave frequencies, Phys. Rev. B **93**, 224430 (2016).

[29] S. R. Etesami, L. Chotorlishvili, and J. Berakdar, Spectral characteristics of time resolved magnonic spin Seebeck effect, Appl. Phys. Lett. **107**, 132402 (2015).

[30] M. Agrawal, V. I. Vasyuchka, A. A. Serga, A. Kirihara, P. Pirro, T. Langner, M. B. Jungfleisch, A. V. Chumak, E. T. Papaioannou, and B. Hillebrands, Role of bulk-magnon transport in the temporal evolution of the longitudinal spin-Seebeck effect, Phys. Rev. B **89**, 224414 (2014).

[31] B. L. Giles, Z. Yang, J. S. Jamison, and R. C. Myers, Long-range pure magnon spin diffusion observed in a nonlocal spin-Seebeck geometry, Phys. Rev. B **92**, 224415 (2015).

[32] H. L. Wang, C. H. Du, Y. Pu, R. Adur, P. C. Hammel, and F. Y. Yang, Large spin pumping from epitaxial Y3Fe5O12 thin films to Pt and W layers, Phys. Rev. B **88**, 100406 (2013).

[33] H. L. Wang, C. H. Du, Y. Pu, R. Adur, P. C. Hammel, and F. Y. Yang, Scaling of Spin Hall Angle in 3d, 4d, and 5d Metals from Y3Fe5O12/Metal Spin Pumping, Phys. Rev. Lett. **112**, 197201 (2014).

[34] J. T. Brangham, K.-Y. Meng, A. S. Yang, J. C. Gallagher, B. D. Esser, S. P. White, S. Yu, D. W. McComb, P. C. Hammel, and F. Yang, Thickness dependence of spin Hall angle of Au grown on Y3Fe5O12 epitaxial films, Phys. Rev. B **94**, 054418 (2016).

[35] T. Kikkawa, K. Uchida, Y. Shiomi, Z. Qiu, D. Hou, D. Tian, H. Nakayama, X.-F. Jin, and E. Saitoh, Longitudinal Spin Seebeck Effect Free from the Proximity Nernst Effect, Phys. Rev. Lett. **110**, 067207 (2013).

[36] B. F. Miao, S. Y. Huang, D. Qu, and C. L. Chien, Absence of anomalous Nernst effect in spin Seebeck effect of Pt/YIG, AIP Adv. **6**, 015018 (2016).

[37] D. Ellsworth, L. Lu, J. Lan, H. Chang, P. Li, Z. Wang, J. Hu, B. Johnson, Y. Bian, J. Xiao, R. Wu, and M. Wu, Photo-spin-voltaic effect, Nat. Phys. **12**, 861 (2016).

[38] F. Guo, J. M. Bartell, D. H. Ngai, and G. D. Fuchs, Phase-Sensitive Imaging of Ferromagnetic Resonance Using Ultrafast Heat Pulses, Phys. Rev. Appl. **4**, 044004 (2015).

[39] See Supplemental Material at [URL will be inserted by publisher] for details of the design and characterization of the magnetothermal microscope as well as discussion related to the

determination of the temperature increase and the image analysis.

[40] J. H. Weaver, Optical properties of Rh, Pd, Ir, and Pt, Phys. Rev. B **11**, 1416 (1975).

[41] A. D. Rakić, A. B. Djurišić, J. M. Elazar, and M. L. Majewski, Optical properties of metallic films for vertical-cavity optoelectronic devices, Appl. Opt. **37**, 5271 (1998).

[42] E. W. M. Haynes, editor , *CRC Handbook of Chemistry and Physics*, 97th Edition (CRC Press/Taylor & Francis, Boca Raton, FL).

[43] A. M. Hofmeister, Thermal diffusivity of garnets at high temperature, Phys. Chem. Miner. **33**, 45 (2006).

[44] A. E. Clark and R. E. Strakna, Elastic Constants of Single-Crystal YIG, J. Appl. Phys. **32**, 1172 (1961).

[45] S. Wemple, S. Blank, J. Seman, and W. Biolsi, Optical properties of epitaxial iron garnet thin films, Phys. Rev. B **9**, 2134 (1974).

[46] D. L. Wood and K. Nassau, Optical properties of gadolinium gallium garnet, Appl. Opt. **29**, 3704 (1990).

[47] M. Schreier, T. Chiba, A. Niedermayr, J. Lotze, H. Huebl, S. Geprägs, S. Takahashi, G. E. W. Bauer, R. Gross, and S. T. B. Goennenwein, Current-induced spin torque resonance of a magnetic insulator, Phys. Rev. B **92**, 144411 (2015).

[48] T. Chiba, G. E. Bauer, and S. Takahashi, Current-Induced Spin-Torque Resonance of Magnetic Insulators, Phys. Rev. Appl. **2**, 034003 (2014).

[49] J. Sklenar, W. Zhang, M. B. Jungfleisch, W. Jiang, H. Chang, J. E. Pearson, M. Wu, J. B. Ketterson, and A. Hoffmann, Driving and detecting ferromagnetic resonance in insulators with the spin Hall effect, Phys. Rev. B **92**, 174406 (2015).

[50] N. Vlietstra, J. Shan, V. Castel, B. J. van Wees, and J. Ben Youssef, Spin-Hall magnetoresistance in platinum on yttrium iron garnet: Dependence on platinum thickness and in-plane/out-of-plane magnetization, Phys. Rev. B **87**, 184421 (2013).

[51] M. Weiler, M. Althammer, M. Schreier, J. Lotze, M. Pernpeintner, S. Meyer, H. Huebl, R. Gross, A. Kamra, J. Xiao, Y.-T. Chen, H. Jiao, G. E. W. Bauer, and S. T. B. Goennenwein, Experimental Test of the Spin Mixing Interface Conductivity Concept, Phys. Rev. Lett. **111**, 176601 (2013).

[52] M. Althammer, S. Meyer, H. Nakayama, M. Schreier, S. Altmannshofer, M. Weiler, H. Huebl, S. Geprägs, M. Opel, R. Gross, D. Meier, C. Klewe, T. Kuschel, J.-M. Schmalhorst, G. Reiss, L. Shen, A. Gupta, Y.-T. Chen, G. E. W. Bauer, E. Saitoh, and S. T. B. Goennenwein, Quantitative study of the spin Hall magnetoresistance in ferromagnetic insulator/normal metal hybrids, Phys. Rev. B **87**, 224401 (2013).

[53] N. Vlietstra, J. Shan, B. J. van Wees, M. Isasa, F. Casanova, and J. Ben Youssef, Simultaneous detection of the spin-Hall magnetoresistance and the spin-Seebeck effect in

platinum and tantalum on yttrium iron garnet, Phys. Rev. B **90**, 174436 (2014).

[54] C. Hahn, G. de Loubens, O. Klein, M. Viret, V. V. Naletov, and J. Ben Youssef, Comparative measurements of inverse spin Hall effects and magnetoresistance in YIG/Pt and YIG/Ta, Phys. Rev. B **87**, 174417 (2013).

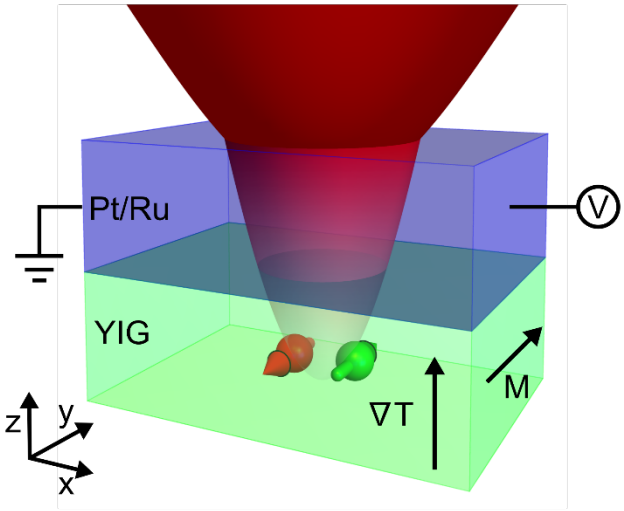

381

382

383 FIG. 1 Schematic of our TRLSSE measurement. A 780 nm, 3 ps pulsed laser, focused to a

384 0.606 μm diameter spot, is used to heat a YIG (20 nm)/Pt(6 nm)/Ru(2 nm) film. The heating

385 from the laser creates a temperature gradient, ∇T_z. The pulsed heating drives a pulsed magnon

386 flux, $\mathbf{J_s}$, from the YIG into the Pt where it is transduced into a pulsed voltage via the ISHE.

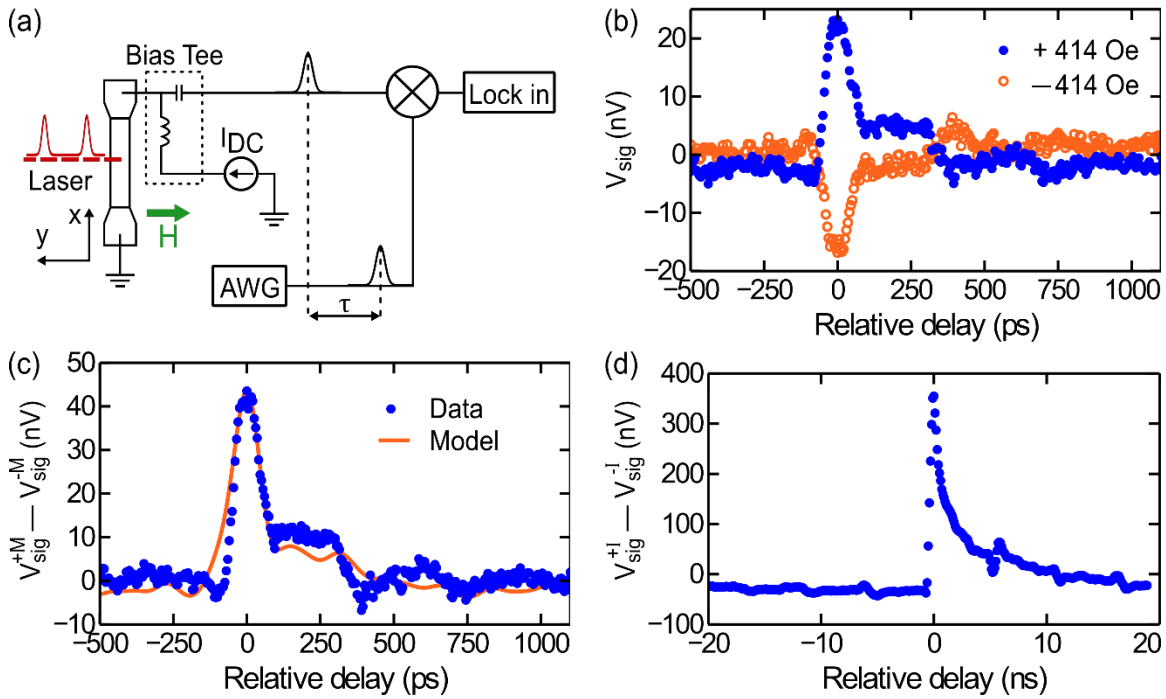

387

388 FIG. 2 (a) Schematic of the LSSE detection circuit used for time-resolved voltage
389 measurements. (b) Time-domain measurement of the LSSE generated voltage in the 2 μm wide
390 wire. The time-varying LSSE signal is measured by electrically mixing the pulsed laser
391 generated voltage with a 100 ps voltage pulse from the AWG. Comparing measurements of the
392 YIG at +414 Oe (filled blue circles) and –414 Oe (open orange circles) shows that the signal
393 depends on the orientation of the magnetic moment. Here d.c. level noise and has been removed.
394 The data was acquired with a lock-in time constant of 500 ms and integration time of 2 s per
395 point. (c) The solid blue circles show the difference between the two curves in (b), The orange
396 line is a model, normalized by the data amplitude, of the signal determined by numerically
397 convolving the calculated thermal gradient with the measured mixing pulse. (d) Difference signal
398 of the temperature dependent voltage V_J measured using +/– 0.5 mA and a 600 ps mixing pulse.
399 In (b-d) we report the voltage as detected at the lock-in after passing through the r.f. mixer, not
400 the LSSE signal at the sample itself.

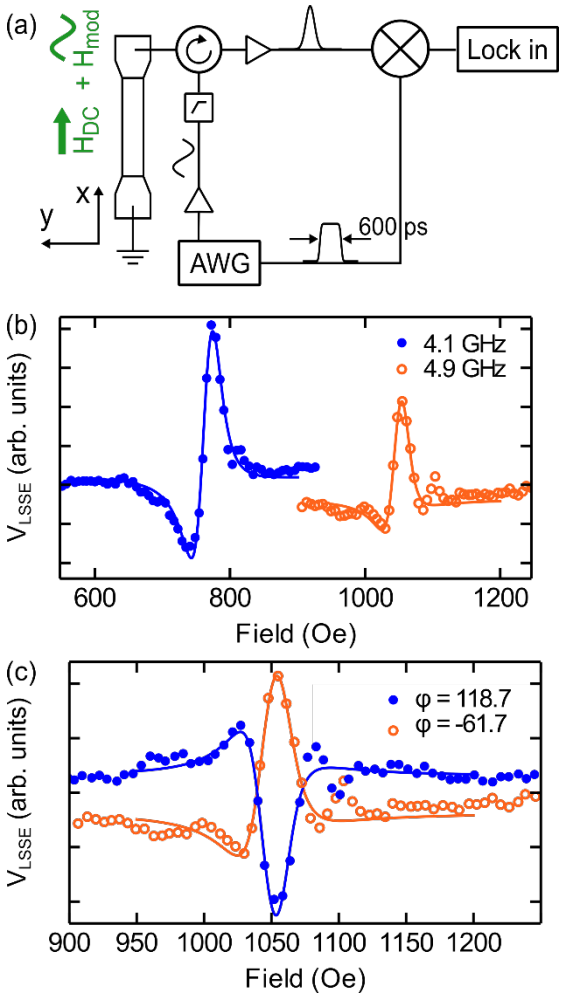

401

402 FIG. 3 Stroboscopic detection of ferromagnetic resonance a) Schematic of measurement circuit
403 for detection of magnetization dynamics in the 2 μm wide wire. b) TRLSSE detected FMR for
404 4.1 GHz (blue, closed circles) and 4.9 GHz (orange, open circles) excitation. The solid lines are a
405 fit to the data using a modified Lorentzian. c) Demonstration of stroboscopic FMR detection in
406 which we measure the response of the YIG driven at phases that differ by 180 degrees. The data
407 was acquired with a lock-in time constant of 1s and integration time of 5 s per point.

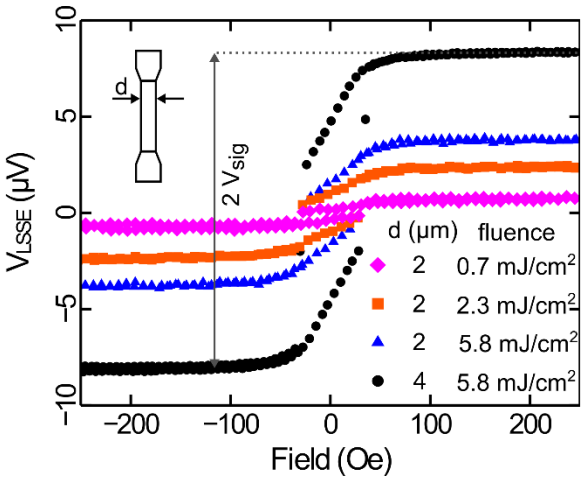

408

409 FIG. 4 Measurement of YIG magnetization with LSSE measuring V_{LSSE} versus external

410 magnetic field for different laser powers and wire widths. For these curves, a DC background

411 was subtracted. The inset shows the wire geometry. We define the signal size to be one-half of

412 the difference in voltage when the magnetization is saturated in opposing directions. The data

413 was acquired with a lock-in time constant of 500 ms and integration time of 2 s per point.

414

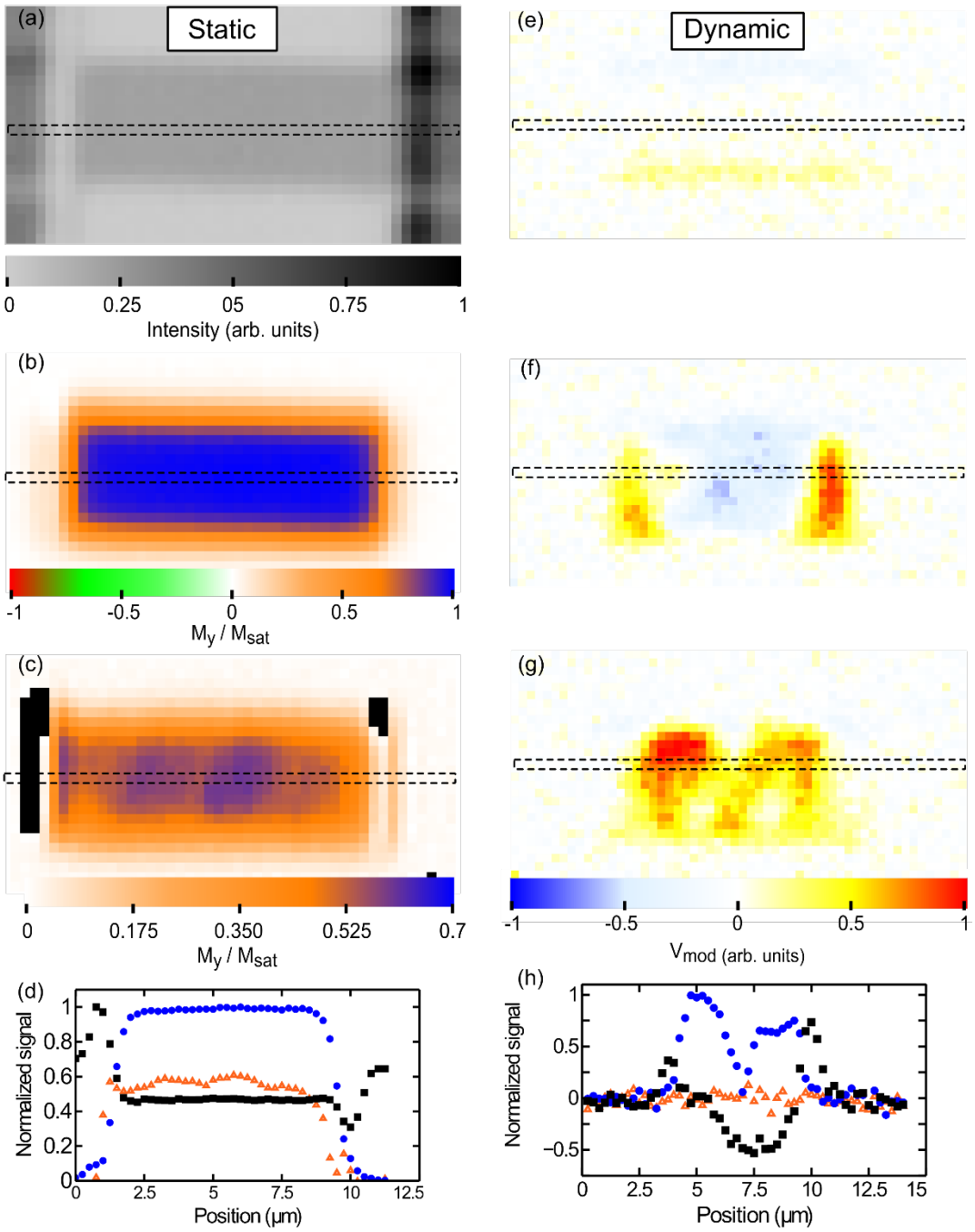

415

416 FIG. 5 Images of the 4 μm wide YIG/Pt wire (a) Reflected light image of the YIG/Pt wire

417 measured with a photodiode at the same time as the LSSE voltage. (b) Background subtracted

418 LSSE voltage at saturated magnetization and (c) remnant magnetization at 4 Oe after saturation.

(d) Line cuts of the 2D scans. The normalized reflection signal is shown with black squares, blue circles represent the saturated magnetization, and the orange triangles represent the magnetization of the remnant state. Note, that in the line cuts the low field line cut is normalized with respect to the saturation magnetization. The right side of the figure represents the raw images of the 4 μm wire at different fields around the resonance: (e) 896 Oe. (f) 1007 Oe, (g) 1025 Oe. Images (e-g) share the same color scale. Line cuts of the images are shown in (h) black squares, blue circles, and orange triangles correspond to the boxed regions of (e), (f), and (g) respectively. For (e-g) the data was acquired with a lock-in time constant of 200 ms and an integration time of 2 s.

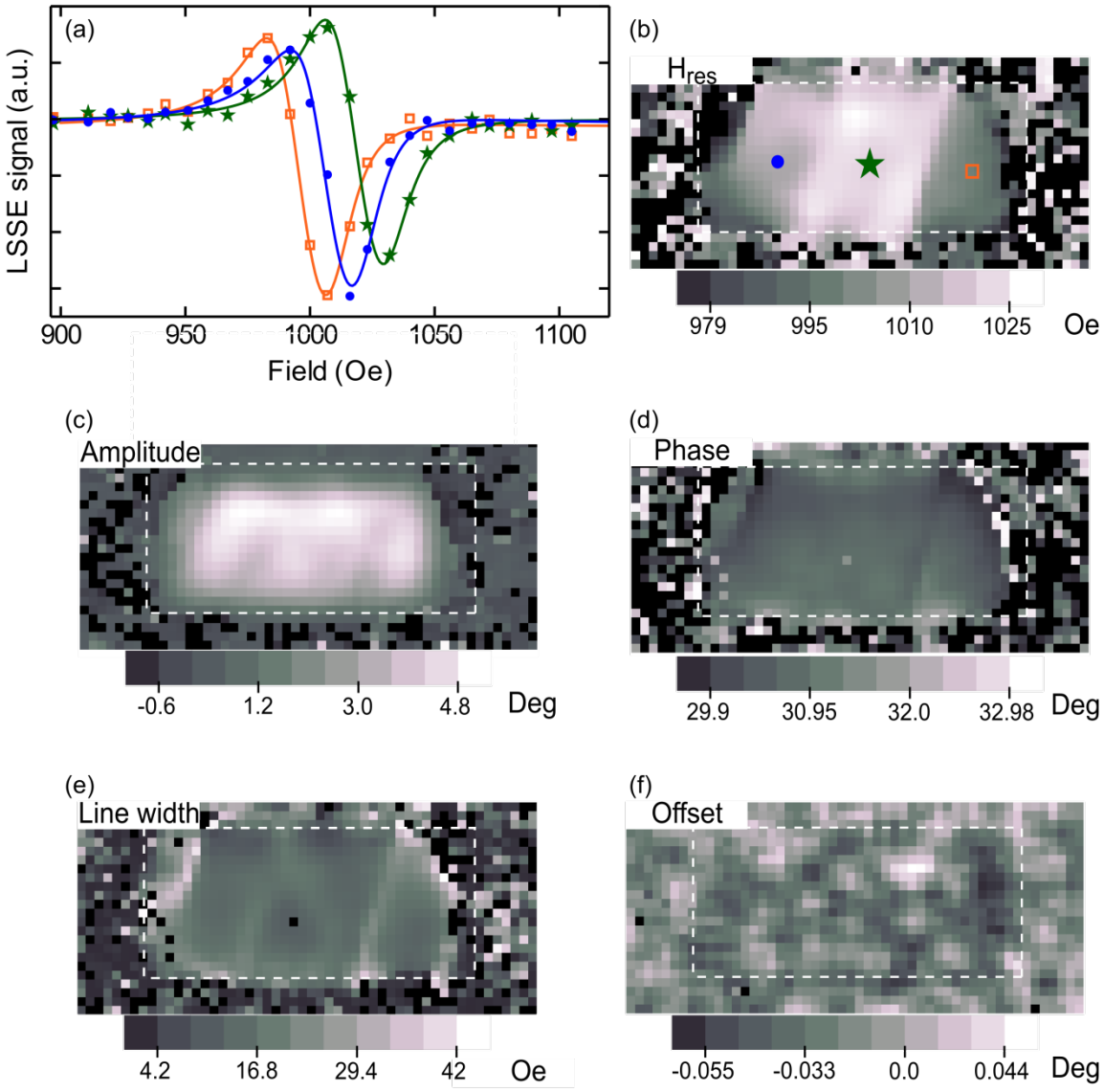

428

429 FIG. 6 Spatial maps of FMR fitting parameters for the 4 μm wide wire. (a) Traces are the pixel
430 values of three points on the sample as a function of magnetic field. b-f) Spatial maps of the
431 FMR fitting parameters made by fitting of the FMR curves at each pixel in the sequence of
432 images measured with LSSE. Before fitting, we correct for image-to-image offset and use a 3x3
433 pixel moving average to smooth the data. (b) Resonance field, the symbols mark the pixels
434 corresponding to the FMR spectra shown in (a). (c) Resonance amplitude, (d) resonance phase,
435 (e) resonance linewidth (f) offset used in the fit.